APPLICATION AND ASSESSMENT OF GPM-BASED NEAR-REAL-TIME SATELLITE PRECIPITATION PRODUCTS IN MONITORING DIURNAL PRECIPITATION VARIATION OVER TAIWAN

Jie Hsu[1] Wan-Ru Huang*[2], and Pin-Yi Liu[2]

[1]PhD Student, Department of Atmospheric Sciences, National Taiwan University
No. 1, Sec. 4, Roosevelt Rd., Taipei 10617, Taiwan
Email: jason8404025@gmail.com

[2]Distinguished Professor, Department of Earth Sciences, National Taiwan Normal University,
No. 88, Sec. 4, Tingchou Rd., Wenshan District, Taipei 11677, Taiwan
Email: wrhuang@ntnu.edu.tw

[2]Research Assistant, Department of Earth Sciences, National Taiwan Normal University,
No. 88, Sec. 4, Tingchou Rd., Wenshan District, Taipei 11677, Taiwan
Email: pinyiliu@ntnu.edu.tw

KEY WORDS: Complex terrain, Diurnal precipitation, Satellite Precipitation, East Asia, Taiwan

ABSTRACT: This study evaluated the performance of four near-real-time (NRT) multiple-satellite precipitation products (MSPPs) from the Global Precipitation Measurement (GPM) mission in depicting the variation in diurnal precipitation from 2017 to 2020, in May to September (MJJAS). The four NRT MSPPs include the V06 of Integrated Multi-satellitE Retrievals for the GPM Early Run (IMERG-E) and Late Run (IMERG-L), and the V07 of Global Satellite Mapping of Precipitation NRT (GSMaP-N) and Gauge-NRT (GSMaP-GN). Two sub-components of diurnal precipitation variation were evaluated, daily mean (Pm) and anomalies (ΔP); ΔP was further separated into diurnal (S1) and semidiurnal (S2) harmonic modes. Compared with surface observations, results show that all NRT MSPPs underestimate Pm and ΔP, but IMERG products are better than GSMaP products in most of the examined spatial characteristics. Temporally, only IMERG-E depicts the phase evolution of both S1 and S2, similar to surface observations. These findings indicate that IMERG-E is the best NRT product for studying the diurnal precipitation characteristics across MJJAS in Taiwan. The general bias in the NRT MSPPs considered in the study in depicting the features examined was attributed to the limitation of passive microwave sensors in illustrating the developing and dissipating stage of diurnal precipitation formation, and to the weakness of infrared precipitation algorithms in detecting warm orographic clouds.

1. INTRODUCTION

1.1 Motivations

Multiple-satellite precipitation products (MSPPs) are an important resource for studying variations in global and regional precipitation. The Tropical Rainfall Measurement Mission (TRMM) was launched in November 1997 to help understand tropical precipitation variations within the water cycle (Huffman et al., 2007). In February 2014, the Global Precipitation Measurement (GPM) Core Satellite was launched (Hou et al., 2014), and new GPM products were developed to continue providing global precipitation observations after completion of the TRMM. Currently, there are two main data sources for GPM-based MSPPs: the Integrated Multi-satellitE Retrievals for GPM (IMERG) (Huffman et al., 2020) provided by the National Aeronautics and Space Administration (NASA) and the Global Satellite Mapping of Precipitation (GSMaP) (Kubota et al., 2007) provided by the Japan Aerospace Exploration Agency (JAXA). Compared with TRMM-based MSPPs (herein referred as TMPA), GPM-based MSPPs have higher spatiotemporal resolution and improved algorithms (Kubota et al., 2007; Huffman et al., 2020). Thus, it is generally expected that GPM-based MSPPs might provide more reliable precipitation estimates for research. However, this expectation requires many validation efforts. Notably, TMPA is a legacy product that is not being extended; therefore, this study focused on the current GPM-based MSPPs. As all the GPM-based MSPPs incorporate TRMM as the calibrator to provide a data record that extends well before the initiation of GPM, the TRMM record is not lost in IMERG and GSMaP.

1.2 Overview and references to related work

Both IMERG and GSMaP provide near-real-time (NRT) products and post-real-time (PRT) products, depending on the time latency. IMERG has two NRT products (early and late runs, herein referred as IMERG-E and IMERG-L, respectively) and one PRT product (final run, herein referred as IMERG-F) (Huffman et al., 2020). The release of IMERG-E and IMERG-L is delayed 4 h and 14 h after the observation time, respectively (Table 1). In contrast, the release of IMERG-F is delayed by 3.5 months because its production requires adjustment based on monthly gauge data (Huffman et al., 2020). Although the three runs of IMERG products might outperform each other in depicting the precipitation variation over different regions (O et al., 2017; Tang et al., 2020; Huang et al., 2021a), NASA has advised researchers to use IMERG-F for most research purposes (https://gpm.nasa.gov/data/directory). Following this suggestion, many studies have focused on assessing IMERG-F precipitation estimates over various regions (Wang et al., 2017; Huang et al., 2018; O and Kirstetter, 2018; Navarro et al., 2019; Huang et al., 2020; Moazami and Najafi, 2021). For example, Huang et al. (2018) and Huang et al. (2020) assessed the performance of IMERG-F in depicting the precipitation variation over Taiwan, an island of approximately 36000 km^2 and complex orography features (Figure 1), and noted that IMERG-F showed better depiction of the monthly, daily, and diurnal precipitation variation in Taiwan during the warm seasons compared to those during the cold seasons. However, it is necessary to use NRT products when examining the spatiotemporal characteristics of precipitation formation prior to the release of PRT products. Thus, it is also important to determine the capability of IMERG-E and IMERG-L in depicting precipitation variations over various regions (O et al., 2017; Ma et al., 2020; Huang et al., 2021a).

Table 1. Information (including period, spatiotemporal resolution, latency, and morphing algorithm) about the four near-real-time (NRT) multiple satellite precipitation products (MSPPs, hereafter including IMERG-E, IMERG-L, GSMaP-N, and GSMaP-GN) used in this study.

	Period	Spatial resolution	Temporal resolution	Latency	Morphing algorithm
IMERG-E	2000/06-present	0.1°×0.1°	30 min	4 h	forward
IMERG-L	2000/06-present	0.1°×0.1°	30 min	14 h	forward and backward
GSMaP-N	2017/04-present	0.1°×0.1°	1 h	4 h	forward
GSMaP-GN	2017/04-present	0.1°×0.1°	1 h	4 h	forward

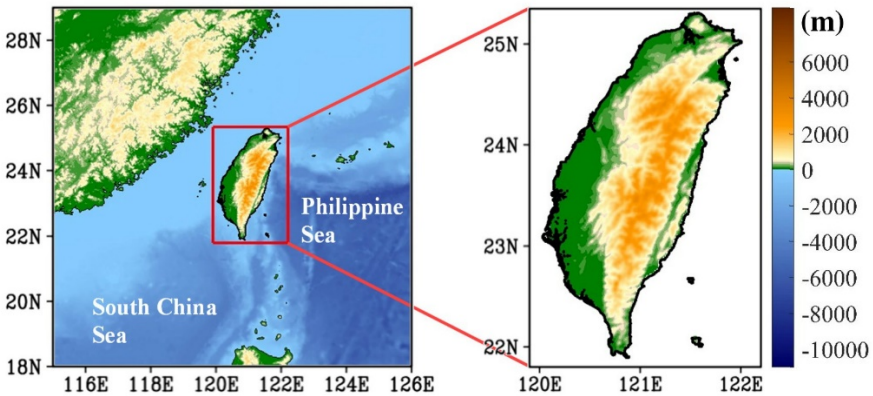

Figure 1. Geographic location and topography of Taiwan. The topographic information was obtained from https://www.ngdc.noaa.gov/mgg/global/.

In contrast to IMERG, GSMaP has two PRT products (GSMaP-MVK and GSMaP-Gauge; herein referred as GSMaP-M and GSMaP-G, respectively) with a 3-day latency and two NRT products (GSMaP-NRT and GSMaP-Gauge-NRT; herein referred as GSMaP-N and GSMaP-GN, respectively) with a 4 h latency (Kubota et al., 2020). Most studies evaluating the ability of GSMaP products have mainly focused on the assessment of PRT products across various regions (Tian et al., 2010; Prakash et al., 2015; Hur et al., 2016; Setiawati and Miura, 2016; Setiyoko et al., 2019; Trinh-Tuan et al., 2019; Huang et al., 2020). In addition, some studies have compared the differences between the PRT products of IMERG and GSMaP (Reddy et al., 2019; Salles et al., 2019; Huang et al., 2020; Liu et al., 2020). For Taiwan, Huang et al. (2020) compared the GPM-based PRT products (including IMERG-F and GSMaP-G) in depicting the summer diurnal precipitation formation, and found that IMERG-F outperforms GSMaP-G in both estimations of quantitative precipitation and depiction of phase evolution. However, to the best of our knowledge, it is unclear whether this conclusion is also

valid when juxtaposing GPM-based NRT products (including IMERG-E, IMERG-L, GSMaP-N, and GSMaP-GN) in depicting the diurnal precipitation formation over Taiwan.

1.3 Aims

Notably, the monthly and daily means of GPM-based MSPPs for both PRT and NRT products over Taiwan have been examined in our previous studies (Huang et al., 2018; Huang et al., 2021a, 2021b). Further, the diurnal variation of GPM-based PRT products has also been examined (Huang et al., 2020). In contrast from previous studies (Huang et al., 2018; Huang et al., 2020; Huang et al., 2021a, 2021b), this study aimed to examine the time scale of hourly precipitation variation to compare the NRT products of IMERG and GSMaP. In particular, we focused on the active months for the variation in diurnal precipitation in Taiwan (identified later in Figure 2). Formation of diurnal precipitation has been commonly observed over Taiwan (Chen et al., 1999; Chen and Chen, 2003; Kerns et al., 2010; Huang and Wang, 2014; Huang and Chang, 2018). Sometimes, extreme diurnal precipitation formation can lead to local flooding events (Lin et al., 2011). Because NRT MSPPs are an important source for quickly examining the characteristics and causes of diurnal precipitation formation over Taiwan, related assessments are necessary prior to conducting further research.

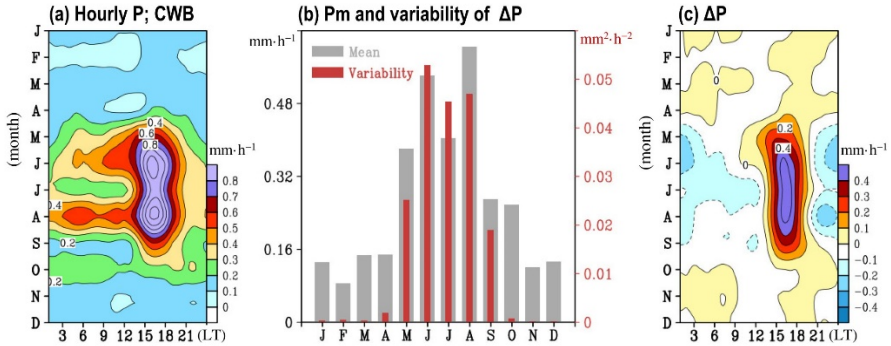

Figure 2. (a) Temporal evolution of hourly precipitation (denoted as P) area-averaged over Taiwan extracted from the Taiwan Central Weather Bureau (CWB) data for each specific month (J to D denotes January to December), averaged over the period from April 2017 to September 2020. LT represents local time. (c) As shown in (a), but for the anomalies of P (ΔP), which obtained by removing the daily mean (Pm) from (a). (b) Calculated from (a) and (c), but for Pm (gray bar) and diurnal variability in ΔP (red bar) for each month.

The objective of this study is not to identify new precipitation features from surface observations, but to use the well-known surface precipitation features as a reference base to evaluate the unknown performance of GPM-based NRT MSPPs. The remainder of this paper is organized as follows. The data and methodology are described in Section 2. Section 3 presents our results on diurnal precipitation evaluation. The causes of the MSPP bias in depicting diurnal precipitation are discussed in Section 4, followed by the conclusions in Section 5.

2. DATA AND METHODOLOGY

2.1 Precipitation Data

This study examined four GPM-based NRT MSPPs (IMERG-E, IMERG-L, GSMaP-N, and GSMaP-GN) from the latest versions of IMERG (V06) and GSMaP (V07). The information regarding the spatiotemporal resolution and available time periods of these MSPPs is presented in Table 1. The analyses focused on the overlapping data periods from April 2017 to September 2020. For comparison, the half-hourly resolutions of IMERG-E and IMERG-L were accumulated to produce hourly resolution data. As described by Huang et al. (2018), we used the gridded surface observed precipitation data generated from 436 rain gauges provided by the Taiwan Central Weather Bureau (herein referred as CWB data) as a reference for comparison. The resolution of CWB data was 0.1° × 0.1° in spatial and hourly temporal intervals.

The detailed information on IMERG V06 can be found in Tan et al. (2019) and Huffman et al. (2020). In general, the production procedures of IMERG products included the following steps: (1) the gridded passive microwave (PMW) precipitation estimates from a network of partner satellites in the GPM constellation were generated using the Goddard profiling algorithm (Kummerow et al., 2015); (2) the precipitation estimates were then applied to the Precipitation Estimation from Remotely Sensed Information Using Artificial Neural Networks—Cloud Cluster System (PERSIANN-CCS) algorithm (Hong et al., 2004; Nguyen et al., 2018) with calibration using the merged PMW; (3) the precipitation estimates were propagated based on vertically integrated vapor; and (4) the Kalman filter approach was applied (Joyce and Xie, 2011). In V06, both IMERG-E and IMERG-L used the Goddard Earth Observing System Forward Processing (GEOS FP) forecast product to derive motion vectors (Tan et al., 2019). However, IMERG-E only applied forward

propagation across time, whereas IMERG-L used both forward and backward propagation across time (Huffman et al., 2020).

The detailed information on GSMaP V07 can be found in Mega et al. (2019) and Kubota et al. (2020). The production procedures of GSMaP V07 generally comprised the following steps: (1) the PMW precipitation estimates were derived using GSMaP's own PMW algorithm and were intercalibrated to the combined microwave radar estimates, in which all algorithms were combined from the GPM constellation satellites (Kubota et al., 2020); (2) the combined precipitation estimates were only propagated forward in time using the atmospheric moving vector derived from infrared (IR) data, and (3) the Kalman filter approach was applied to refine the prediction based on the relationship between the IR brightness, temperature, and surface rainfall rate (Ushio et al, 2009; Kubota et al., 2020). Among GSMaP NRT MSPPs, GSMaP-N was adjusted using a system model with parameters calculated from GSMaP-G data over the past 30 days, to produce GSMaP-GN (Mega et al., 2019; Kubota et al., 2020; Tashima et al., 2020). The difference between GSMaP NRT MSPPs is that the adjustment of GSMaP-GN applied over land, and the precipitation rate estimated over the ocean using GSMaP-GN is the same as that estimated using GSMaP-N.

2.2 Methods

For comparison between CWB and a selected satellite precipitation product (SPP), the correlation coefficient (CC) and root mean square error (RMSE) were calculated using equations (1) and (2), respectively:

$$CC = \frac{\sum_{i=1}^{N}(SPP_i\text{-}SPPm)(CWB_i\text{-}CWBm)}{\sqrt{\sum_{i=1}^{N}(SPP_i\text{-}SPPm)^2}\sqrt{\sum_{i=1}^{N}(CWB_i\text{-}CWBm)^2}}, \quad (1)$$

$$RMSE = \sqrt{\frac{\sum_{i=1}^{N}(SPP_i - CWB_i)^2}{N-1}}, \quad (2)$$

where N is the sample size, CWBm (SPPm) represents the mean of all sample sizes of CWB (SPP), and CWB_i (SPP_i) represents the precipitation estimates for a specific sample of CWB (SPP). Both the temporal correlation coefficient (Tcorr) and spatial correlation coefficient (Scorr) were calculated for later analyses. For Tcorr, the mean status (CWBm and SPPm) in Eq. (1) is determined over time for a selected period (e.g., a month or season). For Scorr, the mean status (CWBm and SPPm) in Eq. (1) is determined over the spatial domain for all spatial grids within the domain. The perfect value for Tcorr and Scorr is 1, and a higher value implies a higher similarity between the CWB and selected SPP. The RMSE was calculated to quantify the difference between the magnitude of the CWB and selected SPP. The perfect value for RMSE is 0, and a lower value suggests a smaller bias of the selected SPP.

To make the evaluation as complete as possible, we separated the diurnal precipitation variation into two parts: daily mean (Pm) and anomalies (ΔP), as in equation (3):

$$P = Pm + \Delta P \quad (3)$$

For Eq. (3), the mean status is determined over time for a selected period (e.g., a month or season). Comparisons between CWB and the four NRT MSPPs were performed for Pm and ΔP. This method has been adopted in many previous studies to better illustrate the diurnal precipitation features (Sato et al., 2009; Huang et al., 2013; Chen et al., 2018). Previous studies have commonly separated the variability of Δ*P* into diurnal [S1(P)] and semidiurnal [S2(P)] harmonic components to examine the diurnal precipitation variation in detail (Dai, 2001; O and Kirstetter, 2018). For example, O and Kirstetter (2018) evaluated the performance of IMERG-F in capturing diurnal [S1(P)] and semidiurnal [S2(P)] variations of ΔP across the United States (US). In this study, we adopted this classic analysis scheme and examined the performance of NRT MSPPs in depicting the spatiotemporal variation of S1(P) and S2(P) across Taiwan. S1(P) and S2(P) were obtained from the first and second harmonic modes of the Fourier analysis, respectively (Storch and Zwiers, 1999). The percentages of S1(P) and S2(P) for explaining the variance of S1(P)+S2(P) were calculated using equation (4):

$$Percentage\ (\%) = \frac{Variance\ of\ S1\ or\ S2}{Variance\ of\ S1 + Variance\ of\ S2} \times 100\% \quad (4)$$

Hereafter, all analyses are presented in Taiwan local time (LT), which is the universal time (UTC) + 8 h. Unless otherwise noted, the climatological fields were obtained from the averaged values during the study period from April 2017 to September 2020.

3. RESULTS

3.1 Area-averaged Precipitation Features

Prior to judging the performance of MSPPs, the frequently examined observational features from the CWB data that serve as the reference base are first illustrated to help explain why the period of May to September (MJJAS), but not a whole year, is the focus of this study. Figure 2a shows the annual evolution of the climatological hourly precipitation area-averaged over Taiwan, as estimated from the CWB data. Visually, a diurnal precipitation maximum occurs in the late afternoon around 16–17 LT during MJJAS (e.g., Huang et al., 2018). By separating the hourly precipitation into the daily mean (Pm; gray bar in Figure 2b) and anomalies (ΔP; Figure 2c), we noted that May to October showed larger amounts of Pm, whereas larger values of variability in ΔP (Figure 2b; red bar) appeared mainly during MJJAS. Temporally, the evolution of ΔP in Figure 2c seems to be separated into two different groups: one is mainly dominated by a maximum/minimum peak within 24 h during MJJAS, and the other is mainly dominated by two maximum/minimum peaks within 24 h from October to April. Similar observational features were also noted in our previous studies (Huang et al., 2018; Huang et al., 2021a, 2021b), but with different periods of analyzed data.

Many studies have examined in diurnal precipitation variation (Haile et al., 2013; Pfeifroth et al., 2016; O and Kirstetter, 2018). It is very important to identify whether the examined data (e.g., satellite precipitation products, model simulation data, etc.) can represent the phase of depicting the time of the diurnal precipitation maximum. Therefore, using the well-known observational features shown in Figure 2, we evaluated the unknown performance of GPM-based NRT MSPPs. The performance of the four NRT MSPPs in depicting the above reference features is shown in Figure 3. Similar to CWB (Figure 2a), all MSPPs captured the hourly precipitation maximum occurring around 16–17 LT during MJJAS (Figure 3a). From January to April (Figure 3a), GSMaP-N and GSMaP-GN seemed to be dominated by two maximum/minimum peaks within 24 h, but this feature was not observed in IMERG-E and IMERG-L. These similarities and differences among MSPPs were more clearly observed in terms of ΔP (Figure 3b). The diurnal evolution of ΔP depicted by all MSPPs (Figure 3b) was similar to that of CWB (Figure 2c) during MJJAS compared to that during other months.

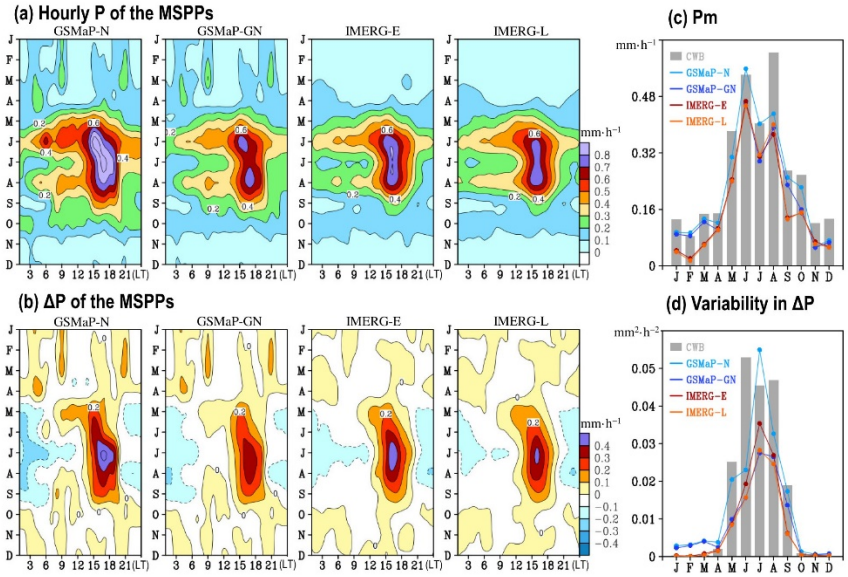

Figure 3. (a) As in Figure 2a, but for the estimation of P (i.e., hourly precipitation) from multiple satellite precipitation products (MSPPs) area-averaged over Taiwan, and averaging over the period from April 2017 to September 2020. The result for GSMaP-N, GSMaP-GN, IMERG-E, and IMERG-L is shown from the left to right. (b) As in (a), but for the estimation of ΔP (i.e., diurnal anomalies of P) from the MSPPs. (c) As in Figure 2b, but for the estimation of Pm (i.e., daily mean of P) extracted from the CWB (gray bar) and MSPPs (colored lines). (d) As in Figure 2b, but for the estimation of diurnal variability in ΔP extracted from the CWB (gray bar) and MSPPs (colored lines).

As for the Pm area-averaged over Taiwan (Figure 3c), all MSPPs can depict the annual cycle with two peaks occurring in June and August, similar to CWB (e.g., Hsu et al., 2021). However, relative to CWB, all MSPPs tended to underestimate the Pm in most months. Similar findings have been reported by Huang et al. (2018, 2020, 2021a, 2021b), but with different time periods and not all the four NRT MSPPs together as in Figure 3c. The statistical values for comparing the time series of Pm in Figure 3c are listed in Table 2. Compared with CWB, all MSPPs have a Tcorr of Pm > 0.9, which is significant at the 95% confidence interval, suggesting a good ability to qualitatively depict the annual

evolution of area-averaged Pm across Taiwan. As for the RMSE of Pm, the value is the smallest for GSMaP-N, whereas the other three MSPPs show a similar performance.

Table 2. Temporal correlation coefficient (hereafter Tcorr) and root mean square error (hereafter RMSE) for comparison between the time series of surface observations from the Taiwan Central Weather Bureau (CWB) and the satellite observations from the four NRT MSPPs shown in Figure 3c. The unit of RMSE is mm·h^{-1}. The highest value of Tcorr and lowest value of RMSE are marked by *.

	GSMaP-N	GSMaP-GN	IMERG-E	IMERG-L
Tcorr for Figure 3c	0.96	0.97	0.97	0.98*
RMSE for Figure 3c	0.06*	0.10	0.11	0.11

Figure 3d shows the hourly ΔP variability estimated from Figure 3b for each specific month. Similar to CWB, all MSPPs depict that the variability in hourly ΔP is larger in MJJAS than in other months. Considering that this study focused on the active months of hourly precipitation variation, the remaining analyses were performed only for MJJAS from 2017–2020. Figure 4a shows the Tcorr for comparing the hourly ΔP of CWB (Figure 2c) and MSPPs (Figure 3b) during a day, and for each individual month of MJJAS. Even though all MSPPs have a value of Tcorr > 0.8, which is significant at a 95% confidence interval, IMERG-E performs the best with a higher Tcorr (Figure 4a) as well as a smaller RMSE (Figure 4b) during most of the examined months. However, this finding is different from that revealed by Pm (Figure 3c), showing that GSMaP-N performs better than other MSPPs in estimating quantitative precipitation during MJJAS. This difference is further discussed in Section 3.2.

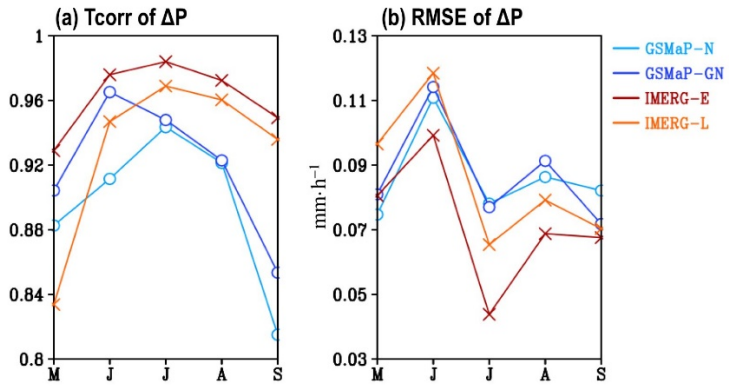

Figure 4. (a) Temporal correlation coefficient (hereafter Tcorr) between the time series of ΔP during a day extracted from Figure 2c (i.e., the CWB) and Figure 3b (i.e., the four NRT MSPPs, hereafter including GSMaP-N, GSMaP-GN, IMERG-E, and IMERG-L) for a specific month from May to September (denoted as M to S). (b) As in (a), but showing the related root mean square error (hereafter RMSE).

The variation of the hourly ΔP area-averaged over Taiwan has demonstrated that it can be mostly explained by its related combination of diurnal and semidiurnal modes [herein S1(P)+S2(P)] (e.g., Huang et al., 2018). Consistent with the report by Huang et al. (2018), we noted from CWB (Figure 5a) that the variation of ΔP is close to S1(P)+S2(P), which also demonstrated a major maximum in the late afternoon and a minor maximum in the early morning. However, different from Huang et al. (2018) used this feature to evaluate the performance of a PRT data, we used this feature to examine the performance of NRT MSPPs. Comparing Figure 5a and Figure 5b, the appearance of the afternoon maximum of S1(P)+S2(P) was markedly dominated by the maximum of S1(P) with contributions by the maximum of S2(P) at around 16–17 LT. In contrast, the appearance of the early morning minor maximum of S1(P)+S2(P) was mainly dominated by the maximum of S2(P) at around 04–05 LT. Similarly, Huang and Chan (2012) examined the ΔP changes over South China (near Taiwan) and concluded that the late afternoon maximum of ΔP was mostly dominated by the S1(P) mode, whereas the early morning minor peak of ΔP was mainly dominated by the S2(P) mode.

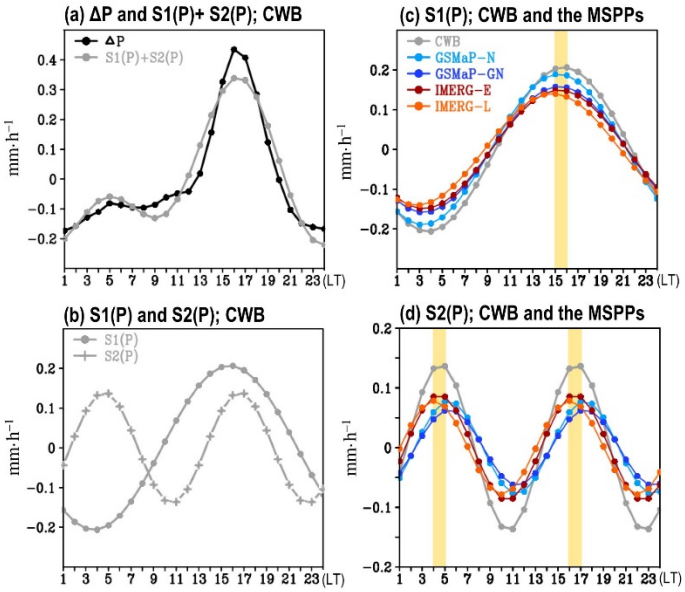

Figure 5. (a) Temporal evolution of ΔP (black line) extracted from the CWB data area-averaged over Taiwan, and averaged over the period of May to September (MJJAS) during 2017 to 2020. In (a), the gray line represents the related combination of the diurnal and semidiurnal harmonic modes of ΔP [denoted as S1(P)+S2(P)]. (b) is the individual component of S1(P) and S2(P) from (a). (c) As in (b), but for S1(P) extracted from CWB and the four NRT MSPPs. The yellow bar represents the timing (two continuous hours) for the maximum value of CWB. (d) As in (c), but for S2(P).

Figure 5c shows the comparison between CWB and the four NRT MSPPs for the temporal evolution of the S1(P) area-averaged over Taiwan and averaged during 2017–2020 MJJAS. For comparison, the timing of occurrence for the observed S1(P) maximum of CWB at 15–16 LT is highlighted using a yellow bar. Overall, most MSPPs show a phase evolution of S1(P) similar to CWB; however, IMERG-L seems to shift the maximum/minimum timing by approximately 1 h earlier than that of the CWB. For S2(P) (Figure 5d), only IMERG-E successfully captured the phase, similar to CWB (occurrence timing of CWB's maximum values highlighted by yellow bars). In contrast, relative to CWB, the two GSMaP products showed delayed maximum peaks, whereas IMERG-L showed advanced maximum peaks for S2(P). Together, these results indicate that IMERG-E has the best performance among MSPPs in capturing the temporal evolution of S1(P)+S2(P) (Figure 6). Indeed, by calculating the Tcorr and RMSE between CWB and MSPPs in Figure 6, the statistical results (Table 3) show that IMERG-E has the largest Tcorr and smallest RMSE, confirming its superiority over other MSPPs. The possible causes for bias in MSPPs, depicting the phase evolution of S1(P) and S2(P), are discussed in Section 4.

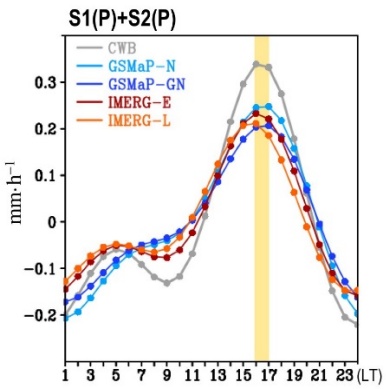

Figure 6. The comparison between CWB and the four NRT MSPPs in capturing the temporal variation of the combination of S1(P) (obtained from Figure 5c) and S2(P) (obtained from Figure 5d). The yellow bar represents the timing (two continuous hours) for the maximum value of CWB.

Table 3. As in Table 2, but is the result of Tcorr and RMSE for comparing time series of CWB and the four NRT MSPPs shown in Figure 6. The unit of RMSE is $mm \cdot h^{-1}$. The highest value of Tcorr and lowest value of RMSE are marked by *.

	GSMaP-N	GSMaP-GN	IMERG-E	IMERG-L
Tcorr for Figure 6	0.95	0.95	0.99*	0.96
RMSE for Figure 6	0.06*	0.07	0.06*	0.07

Figure 6 also shows that IMERG products are better than GSMaP products in capturing the early morning minor peak, but only IMERG-E captures the right phase of S2(P) (Figure 5d). This might be partly attributable to the relatively better performance of IMERG products compared to GSMaP products in depicting the contribution of S1(P) and S2(P), respectively, to the variability in S1(P)+S2(P). To confirm this hypothesis, we calculated the percentage of variability in S1(P)+S2(P) explained by S1(P) and S2(P), respectively, using equation (4). As shown in Table 4, when compared to CWB, GSMaP products have a clear bias in underestimating the contribution of S2(P) to S1(P)+S2(P). This could lead to GSMaP products being less capable of depicting the early morning maximum of S1(P)+S2(P) (Figure 6). Among the four NRT MSPPs, IMERG-E had less bias in determining the respective contribution of S1(P) and S2(P) to S1(P)+S2(P) (Table 4), likely leading to its better ability to represent the phase evolution of S1(P)+S2(P) (Figure 6 and Table 3).

Table 4. The contribution of S1(P) (Figure 5c) and S2(P) (Figure 5d) to the variability in S1(P)+S2(P) (Figure 6), calculated using equation (4) for CWB and the four NRT MSPPs. The contribution is indicated by percentage (%).

	CWB	GSMaP-N	GSMaP-GN	IMERG-E	IMERG-L
S1(P)'s contribution	68.8%	85.5%	86.1%	74.0%	76.2%
S2(P)'s contribution	31.2%	14.5%	13.9%	26.0%	23.8%

3.2 Spatial Features

Thus far, this study has focused on area-averaged values. To clarify the spatial differences, we constructed a climatological (averaged during 2017–2020 MJJAS) horizontal distribution for the occurrence time of the S1(P) maximum during a day (Figure 7a; dotted areas representing the phase difference between MSPPs and CWB are greater than one hour). Overall, CWB depicts the S1(P) maximum occurring during 14–18 LT in most of Taiwan, with a time-lagged feature showing that the S1(P) maximum occurred earlier in the west than in the central region, which is earlier than that in the east (e.g., Huang et al., 2018). Compared with CWB, all MSPPs can represent the S1(P) maximum appearing during 14–18 LT over most of Taiwan, but these are incapable of showing the aforementioned time-lagged relationship. Consistent with Figure 5c, IMERG-L shows greater bias (i.e., more dot areas) compared to other MSPPs in depicting the temporal phase of S1(P), especially across eastern Taiwan, where IMERG-L peaks earlier than CWB.

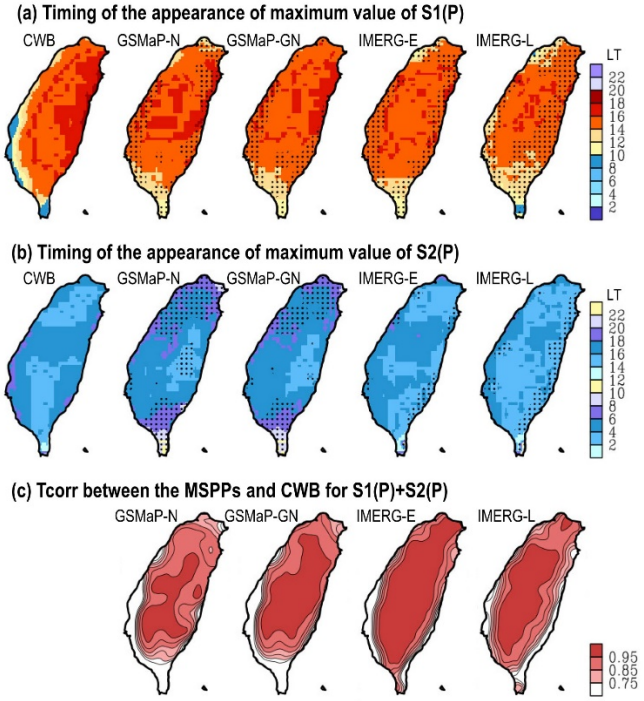

Figure 7. (a) Phase diagram illustrating the occurrence timing of the maximum value of S1(P) extracted from CWB and the four NRT MSPPs, averaged during the 2017–2020 MJJAS. (b) As in (a), but for S2(P). In (a)-(b), the dotted areas representing the phase difference between CWB and the selected SPP are greater than one hour. (c) Grid-to-grid Tcorr for the time series of S1(P)+S2(P) between the MSPPs and CWB, averaged during the 2017–2020 MJJAS.

For S2(P) (Figure 7b), CWB depicts the maximum value that occurred during 04–06 LT and 16–18 LT across most of Taiwan, with the timing over coastal areas being slightly later than that in the mountainous areas. IMERG-E shows the S2(P) phase distribution closest to the CWB (i.e., with less dotted region), whereas IMERG-L performs slightly better than GSMaP products (with more dotted regions). As shown in Figure 5d, the shifting of the S2(P) phase differs between the IMERG-L and GSMaP products, which is in accordance with Figure 7b, showing that IMERG-L has more errors in capturing the S2(P) phase across eastern Taiwan (earlier than CWB), whereas GSMaP products have more errors in capturing the S2(P) phase across western Taiwan (later than CWB). The related grid-to-grid Tcorr between MSPPs and CWB for the time series of S1(P)+S2(P) (Figure 6) is further constructed in Figure 7c. Because of its better ability to capture S1(P) (Figure 7a) and S2(P) (Figure 7b), IMERG-E also has a higher value of Tcorr for S1(P)+S2(P) across most of Taiwan (Figure 7c).

Next, we compared the spatial distribution for the variability in S1(P) (Figure 8a) and S2(P) (Figure 8b), estimated from CWB and MSPPs during 2017–2020 MJJAS. As shown in Figure 8a, the S1(P) variability in CWB is larger over the western mountain slope, where the windward side of the summer monsoon flows (e.g., Chen and Chen, 2003). Relative to CWB, the maximum S1(P) variability in IMERG products shifted slightly to the north, whereas the maximum S1(P) variability in GSMaP products shifted to the west. A similar feature is also shown in Figure 8b, which shows that IMERG products are more capable than GSMaP products in capturing the spatial distribution of S2(P) variability, as in CWB. The evidence supporting this finding is provided in Table 5, which shows higher (smaller) values of Scorr for the comparison between IMERG (GSMaP) products and CWB in Figures 8a–b. With better performance in both S1(P) and S2(P), IMERG products have less bias than GSMaP products in illustrating the spatial distribution of the variability in S1(P)+S2(P) (Figure 8c), and the bias in IMERG-E is slightly smaller than that in IMERG-L.

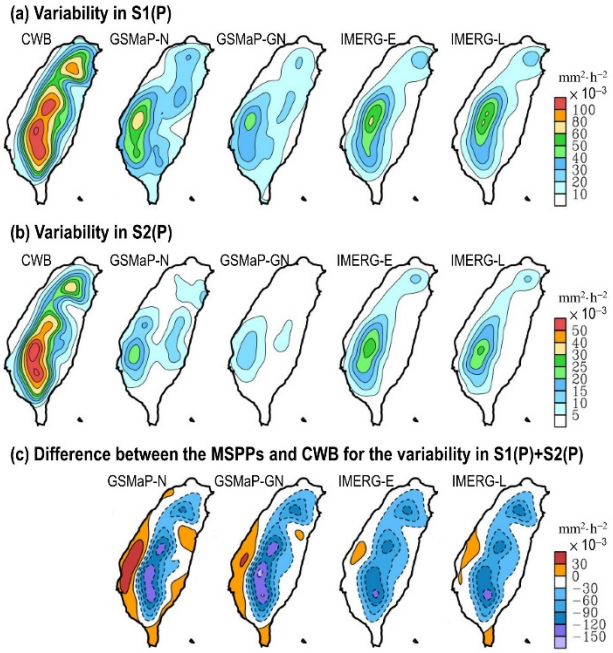

Figure 8. (a) Spatial distribution for the variability in S1(P) extracted from CWB and the four NRT MSPPs, averaged during the 2017–2020 MJJAS, (b) As in (a), but for S2(P). (c) Difference between the MSPPs and CWB for the variability in S1(P)+S2(P), averaged during the 2017–2020 MJJAS.

Table 5. Spatial correlation coefficient (hereafter Scorr) for comparison between CWB and the four NRT MSPPs shown in Figure 8.

	GSMaP-N	**GSMaP-GN**	**IMERG-E**	**IMERG-L**
Scorr for S1(P)	0.30	0.40	0.82	0.80
Scorr for S2(P)	0.22	0.36	0.83	0.82

The spatial distribution of Pm estimated by CWB and MSPPs averaged during 2017–2020 MJJAS was also examined (Figure 9a). Although all MSPPs captured the maximum Pm appearing over southern Taiwan, the patterns of IMERG products (with Scorr > 0.8) were more similar to CWB (Table 6). Among MSPPs, GSMaP-N was the worst (with the smallest value of Scorr) in illustrating the spatial distribution of Pm. This differed from the earlier conclusion that GSMaP-N is the best product for estimating the area-averaged value of Pm (Figure 3c). To further clarify this finding, the spatial differences between the Pm values of the MSPPs and CWB are plotted in Figure 9b. Quantitatively, all MSPPs underestimated the Pm over mountainous regions. However, over the plain areas, GSMaP-N showed a more noticeable overestimation of Pm. As a result of cancellation between overestimation and underestimation, GSMaP-N showed smaller errors in depicting the Pm area-averaged over Taiwan (Table 6).

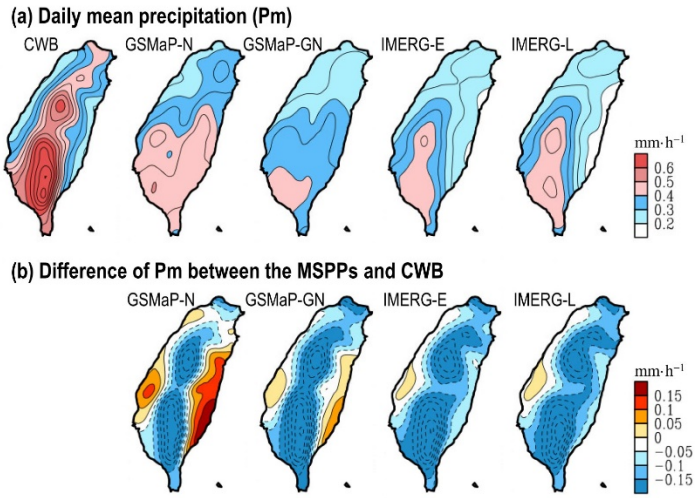

Figure 9. (a) Spatial distribution of daily mean precipitation (Pm) extracted from CWB and the four NRT MSPPs, averaged during the 2017–2020 MJJAS. (b) Spatial difference between the MSPPs and CWB from (a).

Table 6. Statistical values for comparing CWB and the four NRT MSPPs in Figure 9a, including the Scorr and the value of daily mean precipitation (Pm) area-averaged over Taiwan. The unit of Pm is mm·h^{-1}.

	CWB	GSMaP-N	GSMaP-GN	IMERG-E	IMERG-L
Scorr	×	0.44	0.57	0.82	0.82
Pm (area-averaged)	0.44	0.39	0.32	0.31	0.31

The scatter diagram of the original hourly precipitation (P = Pm + ΔP) for comparing the MSPPs and CWB over Taiwan during 2017–2020 MJJAS was further examined (Figure 10). GSMaP-N (Figure 10a) has systematic errors in overestimating weaker precipitation events (spread in the top left) but underestimating stronger precipitation events. Unlike GSMaP-N, GSMaP-GN (Figure 10b) seems to have a criterion of maximum hourly precipitation equal to approximately 30 mm·h^{-1} Therefore, GSMaP-GN underestimated the heavy precipitation events observed by CWB (>30 mm·h^{-1}), explaining why the value of Pm in GSMaP-GN is smaller than that in GSMaP-N (Figure 9a). However, from the related statistical values of CC and RMSE (given in Figures 10a–b), we noted that GSMaP-GN (with larger CC and smaller RMSE) is better than GSMaP-N in the quantitative estimation of hourly precipitation across Taiwan. Unlike GSMaP products, the scatter diagram distributions in IMERG-E (Figure 10c) and IMERG-L (Figure 10d) are more similar, and no clear limitation of the maximum value is found in IMERG products. Further examination of CC and RMSE suggested that IMERG products (with larger CC and smaller RMSE) are better than GSMaP products, with IMERG-E (CC = 0.52, RMSE = 1.79 mm·h^{-1}) being slightly better than IMERG-L (CC = 0.51, RMSE = 1.80 mm·h^{-1}). In summary, all analyzed features suggest that IMERG-E outperforms the other three NRT MSPPs in depicting the hourly precipitation variation over Taiwan.

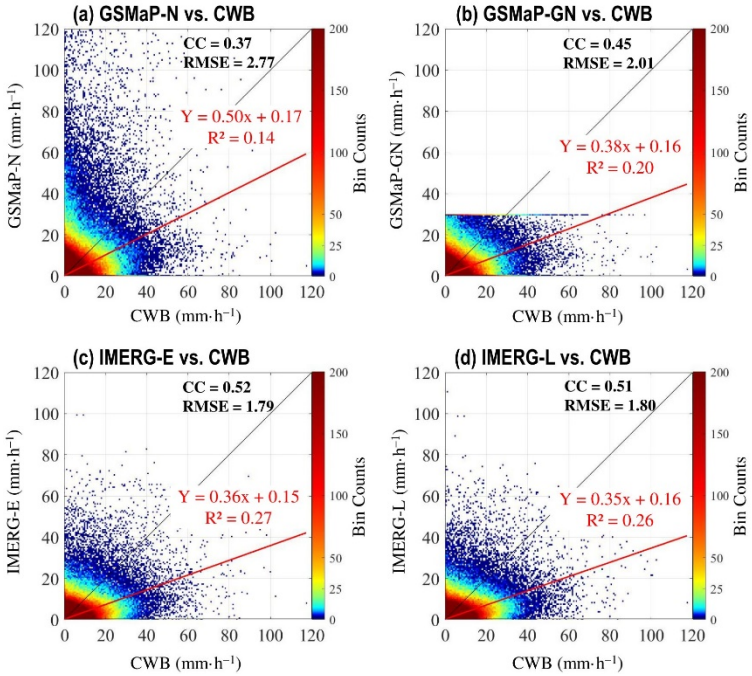

Figure 10. (a) Scatter plot for the comparison of hourly precipitation between CWB (x-axis) and GSMaP-N (y-axis) for all spatial grids over Taiwan during the 2017–2020 MJJAS. The related statistical values show the coefficient of determination (R^2), correlation coefficient (CC), and RMSE; the equation of linear regression (red line) is also provided. The black line represents a 1:1 fit line. The unit of RMSE is mm·h^{-1}. (b) As in (a), but for GSMaP-GN. (c) As in (a), but for IMERG-E. (d) As in (a), but for IMERG-L.

4. DISCUSSION

From Figure 7a, we noted that not all GPM-based NRT MSPPs can capture the time-lagged feature of S1(P), as observed by the CWB. Considering that the bias in the NRT MSPPs might be reflected in the PRT MSPPs (because the latter is developed from the former), we attempted to look for possible explanations of this common bias for GPM-based NRT MSPPs from O and Kirstetter (2018), who evaluated the performance of IMERG-F (a PRT product) in representing the phase of S1(P) over the US. Similar to Figure 7a, O and Kirstetter (2018) found that relative to surface observations, IMERG-F estimated that precipitation appeared late on the west side but early on the east side of Central US. They concluded that this bias was mainly caused by the inability of IMERG-F to represent the developing and dissipating stages of mesoscale convective systems (MCS). In general, the MCS developed in the west, matured in the middle, and decayed in the east of Central US. During the developing and dissipating stages, different phases of water (ice particles, liquid droplets, and water vapor) exist in clouds; these are called mixed-phase cloud systems. In contrast, during the mature stage, ice particles constitute the main phase of water in clouds. As the detection of precipitation in IMERG (including NRT and PRT products) uses PMW sensors, which are more sensitive to ice particles from the mature stage of MCS, IMERG-F does not represent the right timing of maximum precipitation occurring in mixed-phase cloud systems over the west and east sides of Central US (O and Kirstetter, 2018). This bias in the IMERG-F (i.e., PRT product) may also explain the bias of IMERG-E and IMERG-L (i.e., NRT products) in depicting the timing of S1(P) over the western and eastern coastal regions of Taiwan.

Notably, the GSMaP also used PMW for precipitation detection. Therefore, a similar bias in peaking precipitation late in western Taiwan, but early in eastern Taiwan, was also noted in GSMaP-N and GSMaP-GN. Moreover, this bias is revealed in S1(P) (Figure 7a) as well as in S2(P) (Figure 7b). Yamamoto et al. (2008) also found that the differences in peak time precipitation from satellite sensors are related to the evolution of convection precipitation. From these discussions, we suggest that both IMERG and GSMaP need to further improve satellite precipitation retrieval from the process of cloud microphysics to better detect the phase evolution of S1(P) and S2(P) in the NRT products.

Moreover, as shown in Figure 10b, GSMaP-GN has a cut off maximum hourly precipitation of approximately 30 mm·h^{-1}, which led to greater underestimation of the quantitative Pm estimation in GSMaP-GN than in GSMaP-N (Table 6). Therefore, we suggest that adjusting the precipitation threshold from 30 mm·h^{-1} to a higher value depending on the topography, might help improve the quantitative estimation of GSMaP-GN for hourly precipitation over Taiwan. In fact, through personal communication with a GSMaP-GN production team member (Dr. Takuji Kubota in 2021), we understood that this was their first version of the GSMaP-GN method, due to which they have adopted conservative limits

such as 30 $mm \cdot h^{-1}$. In their development of the next version, they are conducting a trade-off study among 30 $mm \cdot h^{-1}$, 50 $mm \cdot h^{-1}$, 100 $mm \cdot h^{-1}$, and 200 $mm \cdot h^{-1}$ as the upper limit. More details will be reported in the future.

Additionally, for why GPM-based NRT MSPPs tending to quantitatively underestimate the Pm over mountainous areas, we suggest the following possible explanations: (1) the brightness temperature of warm orographic clouds is not trained well by the IR precipitation algorithms (e.g., Bitew and Gebremichael, 2010; Maggioni et al., 2016; Sun et al., 2018; Wang and Yong, 2020), and (2) the ice of warm orographic clouds is too sparse to be detected by the PMW sensor (e.g., Dinku et al., 2007; Huang et al., 2018; O and Kirstetter, 2018; Huang et al., 2020). These weaknesses should be further fixed to obtain better satellite precipitation estimations over the complex terrain of Taiwan.

A possible explanation for why IMERG-E is better than IMERG-L in depicting the hourly precipitation variation over Taiwan is also discussed. Notably, IMERG-E only applied the forward algorithms in time, whereas IMERG-L applied forward as well as backward algorithms in time (Tan et al., 2019; Huffman et al., 2020). As IMERG-E already picks the right phase of S1(P) and S2(P) in Figures 5c–d, additional application of backward algorithms in time for IMERG-L might increase its errors in depicting the temporal evolution of diurnal precipitation (O et al., 2017). One factor could be that the forward and backward morphing moves the overpass snapshots forward and backward in time. Thus, the peak in the diurnal cycle may move with the typical flow, and so forward carries the diurnal peak with it, whereas the backward takes the peak in the wrong direction. There are also two more factors possible: (1) the overpass time of a particular satellite might matter, and (2) as the early run has less data, IR has a bigger impact (by personal communication with the IMERG production team member, Dr. George J. Huffman in 2021).

5. CONCLUSIONS

This study aimed to compare the performance of four GPM-based NRT products (GSMaP-N, GSMaP-GN, IMERG-E, and IMERG-L) in depicting the diurnal precipitation variation over Taiwan. Our analyses focused on MJJAS (i.e., months with larger diurnal variability) from 2017 to 2020. We used the gridded data of surface-observed precipitation (CWB data) as a reference for comparison. To make the evaluation as complete as possible, the diurnal precipitation variation was separated into two components: daily mean (Pm) and anomalies (ΔP) using Eq. (3), and ΔP was further separated into diurnal (S1) and semidiurnal (S2) harmonic modes using Fourier analysis. Each of these sub-components of precipitation changes was examined.

Our results show that during MJJAS, all MSPPs tend to underestimate the Pm over most of Taiwan; however, IMERG products (with higher Scorr values) perform better than GSMaP products in depicting the spatial distribution of Pm (Figure 9 and Table 6). For ΔP area-averaged over Taiwan during MJJAS, all MSPPs can capture the occurrence of the late afternoon maximum (Figure 3b), but the performance of IMERG-E (with the largest Tcorr and smallest RMSE in Figure 4) is better than that of other MSPPs. The better ability of IMERG-E to depict the variations in ΔP area-averaged over Taiwan was found to be related to its better ability to represent the variations in S1(P), S2(P), and S1(P)+S2(P). Among all MSPPs, IMERG-E alone peaks the phases of S1(P) and S2(P), area-averaged over Taiwan, similar to the CWB (Figures 5c–d). Therefore, IMERG-E demonstrated the best performance in depicting the temporal phase evolution of S1(P)+S2(P) (Figure 6 and Table 3). The difference between the performance of MSPPs in depicting the area-averaged S1(P) and S2(P) (Figures 5c–d) can be attributed to their ability to capture the spatial distribution of the phases of S1(P) and S2(P) (Figure 7). Spatially, relative to the two GSMaP products, the two IMERG products exhibit distribution in the variability of S1(P) and S2(P) (Figure 8), as well as the distribution of Pm (Figure 9), similar to that in the CWB. In summary, IMERG-E is superior to other MSPPs in depicting the features examined in this study.

The possible causes for general bias in the four examined MSPPs are as follows: (1) the PMW sensor is more sensitive to cloud ice during the mature stage of convective precipitation, but it is difficult to detect the ice of mixed-phase cloud systems during the developing and dissipating stages; (2) warm orographic clouds were not trained well by the IR precipitation algorithms; and (3) the ice particles existing in warm orographic clouds are too sparse to be detected by PMW sensors. These general shortcomings for GPM products need to be improved to obtain better diurnal precipitation detection over Taiwan. To further improve the GSMaP products, we suggest that a cap of maximum hourly precipitation at approximately 30 $mm \cdot h^{-1}$ on GSMaP-GN (Figure 10b) be adjusted to a higher value or be dependent on topography. On the contrary, for IMERG products, we suggest that the extra backward algorithms applied in IMERG-L increased the bias. Notably, other reasons might contribute to the different performance of the MSPPs documented in this study, and these need to be studied further.

ACKNOWLEDGEMENTS

We greatly appreciate the IMERG, GSMaP, and CWB precipitation data provided by NASA (available at https://gpm.nasa.gov/data/imerg), JAXA (available at https://sharaku.eorc.jaxa.jp/GSMaP/), and CWB (available at https://dbar.pccu.edu.tw/), respectively. In addition, we are particularly grateful to Dr. Takuji Kubota and Dr. George J. Huffman for providing comments to help explain the possible factors of bias in the GSMaP data and IMERG data, respectively. This study was supported by the Ministry of Science and Technology of Taiwan under MOST 106-2628-M-003-001-MY4, MOST 110-2111-M-003-003, and MOST 110-2625-M-003-004.

REFERENCES

Bitew M.M., Gebremichael M., 2010. Evaluation through independent measurements: Complex terrain and humid tropical region in Ethiopia, in: Gebremichael, M., Hossain, F. (Eds.), *Satellite Rainfall Applications for Surface Hydrology.* Springer, pp.205–214.

Chen, C.S., Chen, Y.L., 2003. The rainfall characteristics of Taiwan. *Mon. Wea. Rev.* 131, pp. 1323–1341.

Chen, G., Lan, R., Zeng, W., Pan, H., Li, W., 2018. Diurnal variations of rainfall in surface and satellite observations at the monsoon coast (South China). *J. Clim.* 31, pp. 1703–1724.

Chen, S.Y., Huang, W.R., 2017. Evaluation on the performance of TRMM, CMORPH, and PERSIANN in depicting the diurnal precipitation variation in Taiwan. *Atmos. Sci.* 45, pp. 167–191. (In Chinese)

Chen, T.C., Yen, M.C., Hsieh, J.C., Arritt, R.W., 1999. Diurnal and seasonal variations of the rainfall measured by the Automatic Rainfall and Meteorological Telemetry System in Taiwan. *Bull. Am. Meteorol. Soc.* 80, pp. 2299–2312.

Dai, A., 2001. Global Precipitation and Thunderstorm Frequencies. Part II: Diurnal Variations, *J. Clim*. 14(6), pp. 1112-1128.

Dinku, T., Ceccato, P., Grover-Kopec, E., Lemma, M., Connor, S.J., Ropelewski, C.F., 2007. Validation of satellite rainfall products over East Africa's complex topography. *Int. J. Remote Sens.* 28, pp. 1503–1526.

Haile, A.T., Habib, E., Elsaadani, M., Rientjes, T., 2013. Inter-comparison of satellite rainfall products for representing rainfall diurnal cycle over the Nile basin. *Int. J. Appl. Earth Obs. Geoinfo.* 21, pp. 230–240.

Hong, Y., Hsu, K.L., Sorooshian, S., Gao, X., 2004. Precipitation estimation from remotely sensed imagery using an artificial neural network cloud classification system. *J. Appl. Meteorol.* 43, pp. 1834–1853.

Hou, A.Y., Kakar, R.K., Neeck, S., Azarbarzin, A.A., Kummerow, C.D., Kojima, M., Oki, R., Nakamura, K., Iguchi, T., 2014. The global precipitation measurement mission. *Bull. Am. Meteorol. Soc*. 95, pp. 701–722.

Hsu, J., Huang, W. R., Liu, P.Y., Li, X., 2021. Validation of CHIRPS Precipitation Estimates over Taiwan at Multiple Timescales. *Remote Sens.* 13, pp. 254.

Huang, W.R., Chan, J.C.L., 2012. Seasonal variation of diurnal and semidiurnal variation of rainfall over Southeast China. *Clim. Dyn*. 39, pp. 1913-1927.

Huang, W.R., Chan, J.C.L., Au-Yeung, A.Y.M., 2013. Regional climate simulations of summer diurnal rainfall variations over East Asia and Southeast China. *Clim. Dyn*. 40, pp. 1625–1642.

Huang, W., Chang, Y., 2018. Impact of boreal summer intra-seasonal oscillations on warm season diurnal convection activity in Taiwan. *Int. J. Climatol*. 38, pp. 2187–2200.

Huang, W.R., Chang, Y.H., Liu, P.Y., 2018. Assessment of IMERG precipitation over Taiwan at multiple timescales. *Atmos. Res.* 214, pp. 239–249.

Huang, W.R., Liu, P.Y., Chang, Y.H., Liu, C.-Y., 2020. Evaluation and application of satellite precipitation products in studying the summer precipitation variations over Taiwan. *Remote Sens.* 12, pp. 347.

Huang, W.R., Liu, P.Y., Chang, Y.-H., Lee, C.-A., 2021a. Evaluation of IMERG level-3 products in depicting the July to October rainfall over Taiwan: typhoon versus non-typhoon. *Remote Sens.* 13, pp. 622.

Huang, W.R., Liu, P.Y., Hsu, J., Li, X., Deng, L., 2021b. Assessment of near-real-time satellite precipitation products from GSMaP in monitoring rainfall variations over Taiwan. *Remote Sens.* 13, pp. 202.

Huang, W.R., Wang, S.Y., 2014. Impact of land-sea breezes at different scales on the diurnal rainfall in Taiwan. *Clim. Dyn*. 43, pp. 1951–1963.

Huffman, G.J., Bolvin, D.T., Braithwaite, D., Hsu, K., Joyce, R., Kidd, C., Nelkin, E.J., Sorooshian, S., Tan, J., Xie, P., 2020. Algorithm Theoretical Basis Document (ATBD) Version 06: NASA Global Precipitation Measurement (GPM) Integrated Multi-satellitE Retrievals for GPM (IMERG), NASA/GSFC, greenbelt, MD, USA. available online at. https://gpm.nasa.gov/sites/default/files/2020-05/IMERG_ATBD_V06.3.pdf.

Huffman, G.J., Bolvin, D.T., Neklin, E.J., Wolff, D.B., Adler, R.F., Gu, G.J., Hong, Y., Bowman, K.P., Stocker, E.F., 2007. The TRMM multisatellite precipitation analysis (TMPA): quasi-global, multiyear, combined-sensor precipitation estimates at fine scales. *J. Hydrometeorol*. 8, pp. 38–55.

Hur, J., Raghavan, S.V., Nguyen, N.S., Liong, S., 2016. Evaluation of high-resolution satellite rainfall data over Singapore. *Procedia Eng*. 154, pp. 158–167.

Joyce, R.J., Xie, P., 2011. Kalman filter-based CMORPH. *J. Hydrometeorol.* 12, pp. 1547–1563.

Kerns, J.B.W., Chen, Y.L., Chang, M.Y., 2010. The diurnal cycle of winds, rain, and clouds over Taiwan during the Mei-Yu, summer, and autumn rainfall regimes. *Mon. Wea. Rev.* 138, pp. 497–516.

Kubota, T., Aonashi, K., Ushio, T., Shige, S., Takayabu, Y.N., Kachi, M., Arai, Y., Tashima, T., Masaki, T., Kawamoto, N., Mega, T., Yamamoto, M. K., Hamada, A., Yamaji, M., Liu, G., Oki, R., 2020. Global Satellite Mapping of Precipitation (GSMaP) products in the GPM era, in: Levizzani V., Kidd C., Kirschbaum D., Kummerow C., Nakamura K., Turk F. (Eds.), *Satellite Precipitation Measurement. Advances in Global Change Research*, vol 67. Springer, Cham.

Kubota, T., Shige, S., Hashizume, H., Aonashi, K., Takahashi, N., Seto, S., Hirose, M., Takayabu, Y.N., Ushio, T., Nakagawa, K., 2007. Global precipitation map using satellite-borne microwave radiometers by the GSMaP project: production and validation. *IEEE Trans. Geosci. Remote Sens.* 45, pp. 2259–2275.

Kummerow, C.D., David, L.R., Kulie, M., Wang, N.Y., Ferraro, R., Munchak, S.J., Petkovic, V., 2015. The evolution of

the Goddard profiling algorithm to a fully parametric scheme. *J. Atmos. Ocean. Technol.* 32, pp. 2265–2280.
Lin, P.F., Chang, P.L., Jou, J.D., Wilson, J.W., Roberts, R.D., 2011. Warm season afternoon thunderstorm characteristics under weak synoptic-scale forcing over Taiwan island. *Wea. Forecast*. 26, pp. 44–60.
Liu, C.Y., Aryastana, P., Liu, G.R., Huang, W.R., 2020. Assessment of satellite precipitation product estimates over Bali Island. *Atmos. Res.* 244, pp. 105032.
Ma, M., Wang, H., Jia, P., Tang, G., Wang, D., Ma, Z., Yan, H., 2020. Application of the GPM-IMERG Products in Flash Flood Warning: A Case Study in Yunnan, China. *Remote Sens.* 12*,* pp. 1954.
Maggioni, V., Meyers, P.C., Robinson, M.D., 2016. A review of merged high-resolution satellite precipitation product accuracy during the Tropical Rainfall Measuring Mission (TRMM) Era. *J. Hydrometeorol.* 17, pp. 1101–1117.
Mega, T., Ushio, T., Matsuda, M.T., Kubota, T., Kachi, M., Oki, R., 2019. Gauge-adjusted global satellite mapping of precipitation. *IEEE Trans. Geosci. Remote Sens.* 57, pp. 1928–1935.
Moazami, S., Najafi, M.R., 2021. A comprehensive evaluation of GPM-IMERG V06 and MRMS with hourly ground-based precipitation observations across Canada. *J. Hydrol.* 594, pp. 125929.
Navarro, A., García-Ortega, E., Merino, A., Sánchez, J.L., Kummerow, C., Tapiador, F.J., 2019. Assessment of IMERG precipitation estimates over Europe. *Remote Sens.* 11, pp. 2470.
Negri, A.J., Adler, R.F., 1993. An intercomparlson of three satellite infrared rainfall techniques over Japan and surrounding waters. *J. Appl. Meteorol.* 32, pp. 357–373.
Nguyen, P., Ombadi, M., Sorooshian, S., Hsu, K., AghaKouchak, A., Braithwaite, D., Ashouri, H., Rose Thorstensen, A., 2018. The PERSIANN family of global satellite precipitation data: A review and evaluation of products. H*ydrol. Earth Syst. Sci*. 22, pp. 5801–5816.
O, S., Foelsche, U., Kirchengast, G., Fuchsberger, J., Tan, J., Petersen, W.A., 2017. Evaluation of GPM IMERG early, late, and final rainfall estimates using WegenerNet gauge data in southeastern Austria. *Hydrol. Earth Syst. Sci.* 21, pp. 6559–6572.
O, S., Kirstetter, P.E., 2018. Evaluation of diurnal variation of GPM IMERG derived summer precipitation over the contiguous US using MRMS data. *Q. J. Roy. Meteor. Soc.* 144, pp. 270–281.
Pfeifroth, U., Trentmann, J., Fink, A.H., Ahrens, B., 2016. Evaluating satellite-based diurnal cycles of precipitation in the African tropics. *J. Appl. Meteorol. Climatol.* 55, pp. 23–39.
Prakash, S., Mitra, A.K., Rajagopal, E.N., Pai, D.S., 2015. Assessment of TRMM-based TMPA-3B42 and GSMaP precipitation products over India for the peak southwest monsoon season. *Int. J. Climatol*. 36, pp. 1614–1631.
Reddy, M.V., Mitra, A.K., Momin, I.M., Mitra, A.K., Pai, D.S., 2019. Evaluation and inter-comparison of high-resolution multi-satellite rainfall products over India for the southwest monsoon period. *Int. J. Remote Sens.* 40, pp. 4577–4603.
Salles, L., Satgé, F., Roig, H., Almeida, T., Olivetti, D., Ferreira, W., 2019. Seasonal effect on spatial and temporal consistency of the new GPM-based IMERG-v5 and GSMaP-v7 Satellite Precipitation Estimates in Brazil's Central Plateau Region. *Water.* 11*,* pp. 668.
Sato, T., Miura, H., Satoh, M., Takayabu, Y.N., Wang, Y., 2009. Diurnal cycle of precipitation in the tropics simulated in a global cloud-resolving model. *J. Clim.* 22, pp. 4809–4826.
Setiawati, M.D., Miura, F., 2016. Evaluation of GSMaP daily rainfall satellite data for flood monitoring: case study—Kyushu Japan. *J. Geosci. Environ. Prot.* 4, pp. 101.
Setiyoko, A., Osawa, T., Nuarsa, I.W., 2019. Evaluation of GSMaP precipitation estimates over Indonesia. *Int. J. Environ. Geosci.* 3, pp. 26–43.
Sun, Q., Miao, C., Duan, Q., Ashouri, H., Sorooshian, S., Hsu, K.L., 2018. A review of global precipitation data sets: Data sources, estimation, and intercomparisons. *Rev. Geophys.* 56, pp. 79–107.
Tan, J., Huffman, G.J., Bolvin, D.T., Nelkin, E.J., 2019. IMERG V06: Changes to the morphing algorithm. *J. Atmos.Ocean. Technol.* 36, pp. 2471–2482.
Tang, S., Li, R., He, J., Wang, H., Fan, X., Yao, S., 2020. Comparative evaluation of the GPM IMERG early, late, and final hourly precipitation products using the CMPA data over Sichuan Basin of China. *Water.* 12, pp. 554.
Tashima, T.; Kubota, T.; Mega, T.; Ushio, T.; Oki, R., 2020. Precipitation Extremes Monitoring Using the Near-Real-Time GSMaP Product. *IEEE J. Sel. Top. Appl. Earth Observ. Remote Sens.* 13, pp. 5640–5651.
Tian, Y., Peters-Lidard, C.D., Adler, R.F., Kubota, T., Ushio, T., 2010. Evaluation of GSMaP precipitation estimates over the Contiguous United States. *J. Hydrometeorol.* 11, pp. 566–574.
Trinh-Tuan, L., Matsumoto, J., Ngo-Duc, T., Nodzu, M.I., Inoue, T., 2019. Evaluation of satellite precipitation products over Central Vietnam. *Prog. Earth Planet. Sci.* 6, pp. 54.
Ushio, T., Sasashige, K., Kubota, T., Shige, S., Okamoto, K., Aonashi, K., Inoue, T., Takahashi, N., Iguchi, T., Kachi, M., Oki, R., Morimoto, T., Kawasaki, Z. 2009. A Kalman filter approach to the Global Satellite Mapping of Precipitation (GSMaP) from combined passive microwave and infrared radiometric data. *J. Meteorol. Soc. Jpn.* 87A, pp. 137-151.
von Storch, H., Zwiers, F.W., 1999. *Statistical Analysis in Climate Research*, Cambridge University Press: Cambridge, UK, pp. 416-418.
Wang, R., Chen, J., Wang, X., 2017. Comparison of IMERG level-3 and TMPA 3B42V7 in estimating typhoon-related

heavy rain. *Water.* 9, pp. 276.
Wang, H., Yong, B., 2020. Quasi-Global evaluation of IMERG and GSMaP precipitation products over land using gauge observations. *Water*. 12, pp. 243.
Yamamoto, M.K., Furuzawa, F.A., Higuchi, A., Nakamura, K., 2008. Comparison of diurnal variations in precipitation systems observed by TRMM PR, TMI, and VIRS. *J. Clim.* 21, pp. 4011–4028.